

# Full-Wave Analysis of a Split-Cylinder Resonator for Nondestructive Permittivity Measurements

Michael D. Janezic, *Member, IEEE*, and James Baker-Jarvis, *Senior Member, IEEE*

**Abstract**—This paper presents a full-wave analysis of the split-cylinder resonator. We outline a model where the fringing fields are rigorously accounted for and the resonance condition is derived. Using this model, a method for nondestructively measuring the complex permittivity of materials is examined. Measurements of the complex permittivity for low-loss dielectric materials using the split-cylinder resonator agree well with measurements made in a cylindrical cavity. An uncertainty analysis for the complex permittivity is also provided.

**Index Terms**—Dielectric losses, dielectric measurement, nondestructive testing, permittivity measurement, resonators.

## I. INTRODUCTION

THE most precise means of determining the complex permittivity of low-loss dielectrics are resonator methods. Commonly used resonator techniques include the dielectric-post resonator, cylindrical cavity, and the whispering-gallery-mode method [1]. Although usually limited to a single frequency, these resonant methods provide the needed accuracy that broad-band methods lack. A disadvantage of these techniques is that samples must be accurately machined into a symmetrical geometry such as a cylinder. Since sample machining is destructive and sometimes expensive, conventional resonator methods are rarely used for large-scale quality-control purposes.

Kent developed a resonator technique that allows for nondestructive measurements of complex permittivity [2], [3]. This method, the *split-cylinder resonator* technique, uses a cylindrical cavity, which is separated into two halves, as shown in Fig. 1. A sample is placed in the gap between the two shorted cylindrical waveguide sections. A  $TE_{011}$  resonance is excited, and from measurements of the resonant frequency and the quality factor, one determines the complex permittivity of the sample. In terms of sample geometry, the only requirements are that the sample must extend beyond the diameter of the two cavity sections and the sample must be flat. This provides the accuracy of a resonator technique without having to machine the sample.

Unfortunately, having little or no sample preparation comes at the cost of needing a more comprehensive model for the split-cylinder resonator. In conventional resonator methods,

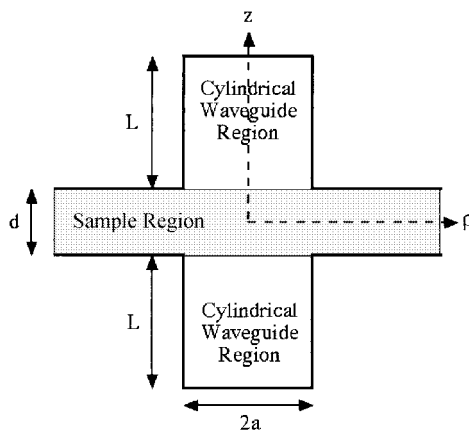


Fig. 1. Cross-sectional diagram of a split-cylinder resonator.

the boundary-value problem is relatively straightforward since the electric and magnetic fields are confined to the sample or within a metallic cavity. However, for the split-cylinder resonator, a gap exists between the two cylindrical waveguide sections, and the electric and magnetic fields extend into the sample outside of the cylindrical waveguide regions.

Kent, in his original model [2], correctly recognized that neglecting the fields in the region of the sample outside of the waveguide sections would lead to a systematic error in the measured permittivity. He initially proposed a correction to the measured permittivity based on a perturbation calculation. Later, Kent and Bell developed an improved approximation to correct the initial model [4].

In contrast, this paper presents a full-wave analysis of the split-cylinder resonator, derived in Section II. In our model, we assume that the fields are confined to regions of the cylindrical waveguide and sample. We also assume the sample is infinite in the radial direction. The model includes the  $TE_{011}$  resonant mode plus evanescent  $TE_{0n}$  modes in the cylindrical waveguide regions. These modes must be included to properly satisfy the boundary conditions at the boundaries between the sample and waveguides. To derive the resonance condition, we applied a Hankel transform with respect to the radial coordinate, reducing the problem to one dimension [5], [6]. We calculated the complex permittivity of several low-loss ceramic materials from measured data. For comparison, we measured the same samples in a conventional cylindrical cavity. Finally, we identify the largest sources of error in the complex permittivity measurement and perform an uncertainty analysis.

Manuscript received September 9, 1998.

The authors are with the National Institute of Standards and Technology, Boulder, CO 80303 USA.

Publisher Item Identifier S 0018-9480(99)07711-X.

## II. DERIVATION OF THE RESONANCE CONDITION

### A. Transverse Fields in the Upper Cavity Region

From the symmetry of the split-cylinder resonator and the assumption that we are exciting only  $TE_{on}$  modes, the electric field in the upper cavity region has only a  $\phi$ -component of the form

$$E_{\phi_u}(\rho, z) = \sum_{n=1}^{\infty} A_n R_n(\rho) Z_{n_u}(z) \quad (1)$$

where  $A_n$  is a constant,  $R_n(\rho)$  is a radial eigenfunction, and  $Z_{n_u}(\rho)$  is a longitudinal function. If we substitute (1) into the vector wave equation

$$\nabla^2 \vec{E} + \omega^2 \mu_0 \epsilon_0 \epsilon'_{ra} \vec{E} = 0 \quad (2)$$

we obtain

$$\frac{1}{R_n} \frac{1}{\rho} \frac{\partial}{\partial \rho} \left[ \rho \frac{\partial R_n}{\partial \rho} \right] - \frac{1}{\rho^2} + k^2 = -\frac{1}{Z_{n_u}} \frac{\partial^2 Z_{n_u}}{\partial z^2} = k_n^2 \quad (3)$$

where  $k^2 = \omega^2 \mu_0 \epsilon_0 \epsilon'_{ra}$ ,  $k_n^2$  is the separation constant,  $\omega$  is the radial frequency, and  $\epsilon'_{ra}$  is the relative permittivity of the air within the cylindrical cavity section. Note that we have assumed a time dependence of  $\exp(j\omega t)$ . We use the method of separation of variables to solve for  $R_n(\rho)$  and  $Z_{n_u}(z)$ . Applying this method to (3), we find

$$E_{\phi_u}(\rho, z) = \sum_{n=1}^{\infty} A_n \left[ C'_n J_1(h_n \rho) + D'_n Y_1(h_n \rho) \right] \cdot \left[ A'_n \sin \left[ k_n \left( L + \frac{d}{2} - z \right) \right] + B'_n \cos \left[ k_n \left( L + \frac{d}{2} - z \right) \right] \right] \quad (4)$$

where  $A'_n$ ,  $B'_n$ ,  $C'_n$ , and  $D'_n$  are constants,  $J_1$  is the Bessel function of the first kind of order one,  $Y_1$  is the Bessel function of the second kind of order one, and  $h_n^2 = k^2 - k_n^2$ . The boundary conditions on the transverse electric field yield

$$E_{\phi_u} \left( \rho, z = L + \frac{d}{2} \right) = 0 \rightarrow Z_{n_u} \left( z = L + \frac{d}{2} \right) = 0, \quad 0 \leq \rho \leq a \quad (5)$$

$$E_{\phi_u}(\rho = 0, z) \text{ is finite} \rightarrow R_n(\rho = 0) \text{ is finite}, \quad (6)$$

$$E_{\phi_u}(\rho = a, z) = 0 \rightarrow R_n(\rho = a) = 0, \quad 0 \leq z \leq L + \frac{d}{2}. \quad (7)$$

It follows that

$$B'_n = 0 \quad (8)$$

$$D'_n = 0 \quad (9)$$

$$h_n = \frac{j_{1,n}}{a} \quad (10)$$

where  $j_{1,n}$  is the  $n$ th zero of  $J_1$ , and (4) reduces to

$$E_{\phi_u}(\rho, z) = \sum_{n=1}^{\infty} A_n R_n(\rho) \sin \left[ k_n \left( L + \frac{d}{2} - z \right) \right] \quad (11)$$

where

$$R_n(\rho) = A'_n C'_n J_1(h_n \rho) = C_n J_1(h_n \rho). \quad (12)$$

From the differential form of Faraday's law

$$\nabla \times \vec{E} = -j\omega \mu_0 \vec{H} \quad (13)$$

and (11) we find the  $\rho$ -component of the magnetic field

$$H_{\rho_u}(\rho, z) = -\frac{1}{j\omega \mu_0} \sum_{n=1}^{\infty} k_n A_n R_n(\rho) \cos \left[ k_n \left( L + \frac{d}{2} - z \right) \right]. \quad (14)$$

In order to find expressions for  $C_n$ , we orthonormalize the radial eigenfunctions  $R_n$ . Substituting (12) into the orthonormalization condition

$$\int_0^a \rho R_n(\rho) R_m(\rho) d\rho = \delta_{mn} \quad (15)$$

we find

$$C_n = \frac{\sqrt{2}}{a J_0(h_n a)} \quad (16)$$

where  $J_0$  is the Bessel function of the first kind of order zero.

To reduce the number of coordinates from two to one, we take the Hankel transforms of  $E_{\phi_u}(\rho, z)$  and of  $H_{\rho_u}(\rho, z)$  with respect to  $\rho$ . The Hankel transform of a function  $f(\rho)$  is defined as

$$\tilde{f}(\zeta) = \int_0^{\infty} \rho' J_1(\zeta \rho') f(\rho') d\rho' \quad (17)$$

and the inverse Hankel transform is

$$f(\rho) = \int_0^{\infty} \zeta J_1(\zeta \rho) \tilde{f}(\zeta) d\zeta. \quad (18)$$

The Hankel transforms of (11) and (14) are

$$\tilde{E}_{\phi_u}(\zeta, z) = \sum_{n=1}^{\infty} A_n \tilde{R}_n(\zeta) \sin \left[ k_n \left( L + \frac{d}{2} - z \right) \right] \quad (19)$$

and

$$\tilde{H}_{\rho_u}(\zeta, z) = -\frac{1}{j\omega \mu_0} \sum_{n=1}^{\infty} k_n A_n \tilde{R}_n(\zeta) \cos \left[ k_n \left( L + \frac{d}{2} - z \right) \right] \quad (20)$$

where

$$\tilde{R}_n(\zeta) = \int_0^a \rho' J_1(\zeta \rho') R_n(\rho') d\rho'. \quad (21)$$

We perform this integration exactly by substituting (12) and (16) into (21) as follows:

$$\tilde{R}_n(\zeta) = \frac{\sqrt{2}}{\zeta^2 - h_n^2} h_n J_1(\zeta a). \quad (22)$$

### B. Transverse Fields in the Lower Cavity Region

As a result of symmetry, the transverse fields in the lower cavity region are

$$\tilde{E}_{\phi_l}(\zeta, z) = \sum_{n=1}^{\infty} A_n \tilde{R}_n(\zeta) \sin \left[ k_n \left( L + \frac{d}{2} + z \right) \right] \quad (23)$$

$$\tilde{H}_{\rho_l}(\zeta, z) = \frac{1}{j\omega\mu_0} \sum_{n=1}^{\infty} k_n A_n \tilde{R}_n(\zeta) \cos \left[ k_n \left( L + \frac{d}{2} + z \right) \right]. \quad (24)$$

### C. Transverse Fields in the Sample Region

In our model, we assume that the sample is infinite in the radial direction and that the magnetic and electric fields can exist anywhere along the sample. However, we assume a conductive ground plane above and below the sample in the region outside the cylindrical waveguide sections. Therefore, any electric or magnetic fields outside the cylindrical waveguide regions must be confined to the sample.

In the sample region, as in the cavity regions, only  $TE_{0n}$  modes are considered. Therefore, the vector wave equation (2) is also satisfied in the sample region as follows:

$$\left[ \frac{1}{\rho} \frac{\partial}{\partial \rho} \left( \rho \frac{\partial}{\partial \rho} \right) + \frac{\partial^2}{\partial z^2} - \frac{1}{\rho^2} + \omega^2 \mu_0 \epsilon_0 \epsilon'_{rs} \right] E_{\phi_s}(\rho, z) = 0. \quad (25)$$

Taking the Hankel transform of (25) and integrating by parts twice, we get

$$\tilde{E}_{\phi_s}(\zeta, z) = S(\zeta) \cos(k_s z) + T(\zeta) \sin(k_s z) \quad (26)$$

where  $k_s^2 = \omega^2 \mu_0 \epsilon_0 \epsilon'_{rs} - \zeta^2$ ,  $\epsilon'_{rs}$  is the relative permittivity of the sample, and  $S$  and  $T$  are coefficients. The split-cylinder resonator symmetry requires that

$$\tilde{E}_{\phi_s} \left( \zeta, z = \frac{d}{2} \right) = \tilde{E}_{\phi_s} \left( \zeta, z = -\frac{d}{2} \right) \quad (27)$$

must hold for all  $0 \leq \zeta \leq \infty$ , and (26) simplifies to

$$\tilde{E}_{\phi_s}(\zeta, z) = S(\zeta) \cos(k_s z). \quad (28)$$

Again, using (13), we determine the transverse magnetic field

$$\tilde{H}_{\rho_s}(\zeta, z) = -\frac{k_s}{j\omega\mu_0} S(\zeta) \sin(k_s z). \quad (29)$$

### D. Resonance Condition

In order to derive the resonance condition, we match boundary conditions. The tangential electric and magnetic fields are continuous at  $z = d/2$

$$\tilde{E}_{\phi_u} \left( z = \frac{d}{2} \right) = \tilde{E}_{\phi_s} \left( z = \frac{d}{2} \right), \quad 0 \leq \zeta \leq \infty \quad (30)$$

$$\tilde{H}_{\rho_u} \left( z = \frac{d}{2} \right) = \tilde{H}_{\rho_s} \left( z = \frac{d}{2} \right), \quad 0 \leq \zeta \leq a. \quad (31)$$

Substituting the transformed electric and magnetic fields into (30)–(31), we find

$$\sum_{n=1}^{\infty} A_n \tilde{R}_n(\zeta) \sin(k_n L) = S(\zeta) \cos \left( k_s \frac{d}{2} \right) \quad (32)$$

$$\sum_{n=1}^{\infty} k_n A_n \tilde{R}_n(\zeta) \cos(k_n L) = k_s S(\zeta) \sin \left( k_s \frac{d}{2} \right). \quad (33)$$

If we take the inverse Hankel transform of (33) with respect to  $\zeta$

$$\begin{aligned} \sum_{n=1}^{\infty} k_n A_n R_n(\rho) \cos(k_n L) \\ = \int_0^{\infty} \zeta J_1(\zeta \rho) k_s S(\zeta) \sin \left( k_s \frac{d}{2} \right) d\zeta. \end{aligned} \quad (34)$$

Multiplying both sides of (34) by  $\rho R_m(\rho)$  and integrating over the interval  $[0, a]$

$$k_m A_m \cos(k_m L) = \int_0^{\infty} \zeta \tilde{R}_m(\zeta) k_s S(\zeta) \sin \left( k_s \frac{d}{2} \right) d\zeta. \quad (35)$$

Using (32), we solve for  $S$  as follows:

$$S(\zeta) = \frac{1}{\cos \left( k_s \frac{d}{2} \right)} \sum_{n=1}^{\infty} A_n \tilde{R}_n(\zeta) \sin(k_n L). \quad (36)$$

Substituting (36) into (35), we find

$$\mathbf{X} \vec{A} = 0 \quad (37)$$

where

$$X_{mn} = -k_m \cos(k_m L) \delta_{mn} + \sin(k_n L) \int_0^{\infty} k_s \tan \left( k_s \frac{d}{2} \right) \cdot \zeta \tilde{R}_m \tilde{R}_n d\zeta \quad (38)$$

and  $\vec{A}$  is a column vector of the coefficients  $A_n$ . The linear system of equations (37) has a nontrivial solution only if

$$\det[\mathbf{X}] = 0 \quad (39)$$

which is the resonance condition. Given the measured resonant frequency, (39) yields the relative permittivity of the sample.

### III. FRINGING FIELDS IN THE SAMPLE REGION

In the previous section, we derived an expression for the electric and magnetic fields in the sample region. In the model, we assumed that the sample was infinite in the radial coordinate and that the fields existed anywhere along the sample. However, since we measure samples with finite diameters, it is important to understand how large the sample diameter must be in order for the assumption of an infinite sample to be valid. Toward this end, we computed the electric field in the sample region. We begin with the transformed electric field (28). Substituting (36) for  $S$  into (28)

$$\tilde{E}_{\phi_s}(\zeta, z) = \frac{1}{\cos \left( k_s \frac{d}{2} \right)} \sum_{n=1}^{\infty} A_n \tilde{R}_n(\zeta) \sin(k_n L) \cos(k_s z). \quad (40)$$

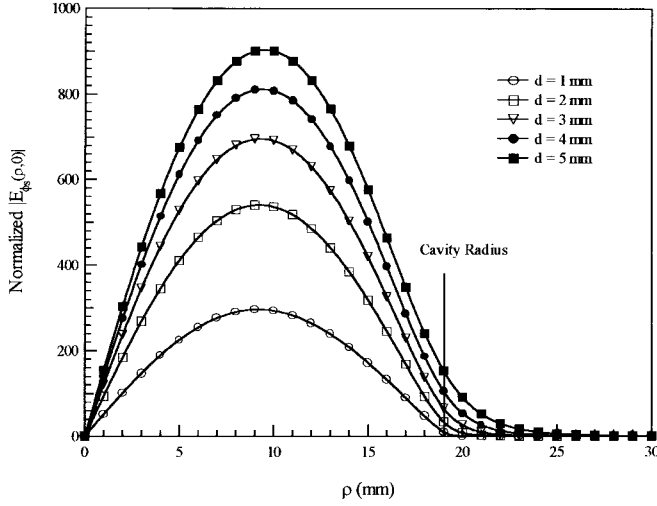


Fig. 2. The magnitude of the normalized electric field  $E_{\phi_s}(\rho, z = 0)$  as a function of  $\rho$  for various values of sample thickness  $d$ . The sample permittivity  $\epsilon'_{rs}$  is ten. The electric field extends beyond the cylindrical waveguide radius and the amount of fringing fields increases as the sample thickness increases.

Taking the inverse Hankel transform of (40), we get

$$E_{\phi_s}(\rho, z) = \sum_{n=1}^{\infty} A_n \sin(k_n L) \int_0^{\infty} \frac{\cos(k_s z)}{\cos\left(k_s \frac{d}{2}\right)} \zeta J_1(\zeta \rho) \cdot \tilde{R}_n(\zeta) d\zeta. \quad (41)$$

Using (41), we computed the normalized electric field in the middle of the sample ( $z = 0$ ) as a function of  $\rho$ , sample thickness, and sample relative permittivity.

Fig. 2 shows the magnitude of the normalized electric field as a function of  $\rho$  and sample thickness for a sample whose relative permittivity is ten. In calculating the electric field, we used a numerical routine that normalized the first coefficient  $A_1$  to one. The results show that some of the electric field in the sample protrudes beyond the cylindrical waveguide radius, especially as the thickness of the sample becomes large. This is consistent with our intuition that the fields in the sample region outside of the cylindrical waveguide are significant. However, the graph also shows that the electric field is negligible when  $\rho$  is approximately 30 mm. Thus, for this cavity, whose radius is approximately 19 mm, we can assume that the sample is infinite in the radial direction in the model without introducing any systematic error if the sample radius is 30 mm and larger.

Fig. 3 shows the magnitude of the normalized electric field as a function of  $\rho$  and sample relative permittivity for a sample whose thickness is 2.5 mm. This also shows that for a wide range of sample relative permittivities, there exists some electric field in the sample beyond the cylindrical waveguide radius. For the various sample permittivities, the value of the normalized electric field at the cavity radius was between 7%–8% of the peak normalized electric field, a value which is not negligible. As was the case in Fig. 2, the electric field is also negligible at values of  $\rho$  larger than 30 mm.

#### IV. COMPLEX PERMITTIVITY MEASUREMENTS

We applied the split-cylinder resonator method to determine the complex permittivity of four low-loss ceramic samples.

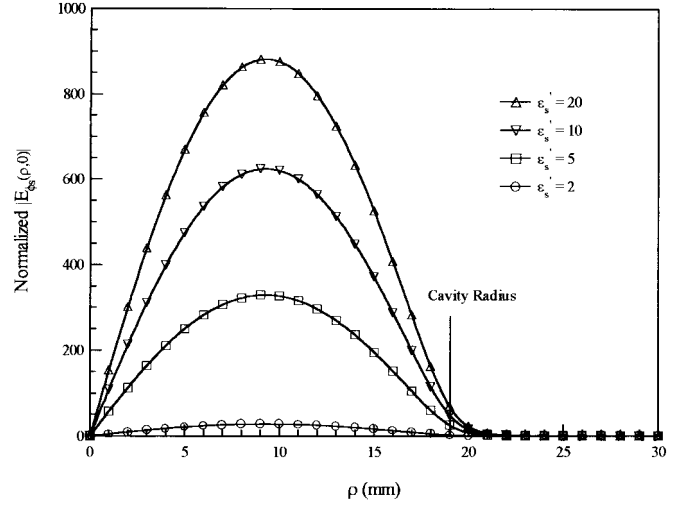


Fig. 3. The magnitude of the normalized electric field  $E_{\phi_s}(\rho, z = 0)$  as a function of  $\rho$  for various values of sample relative permittivity  $\epsilon'_{rs}$ . The sample thickness is 2.5 mm. For all cases, the electric field extends beyond the cylindrical waveguide radius.

TABLE I  
CALCULATED SAMPLE RELATIVE PERMITTIVITY AS A FUNCTION OF THE NUMBER OF  $TE_{0n}$  MODES INCLUDED IN THE MODEL

$TE_{0n}$ Modes	Sample Permittivity $\epsilon'_{rs}$			
	S9	S13	S16	S20
1	9.88	13.62	16.71	20.91
2	9.86	13.60	16.70	20.90
3	9.85	13.59	16.69	20.89
4	9.84	13.59	16.68	20.89
5	9.83	13.58	16.67	20.88
6	9.83	13.57	16.67	20.87
7	9.83	13.57	16.66	20.87
8	9.82	13.57	16.66	20.87

Each sample, approximately 3–5-mm thick with a 60-mm diameter, was placed between the two waveguide sections of the split-cylinder resonator and the resonance curve for the  $TE_{011}$  mode was examined on an automatic network analyzer. An example of a typical resonance is shown in Fig. 4. From the resonance curve, we obtained the resonance frequency  $f_0$  and the quality factor  $Q$ .

In order to determine the real part of the sample permittivity  $\epsilon'_{rs}$ , we use the resonance condition

$$\det[\mathbf{X}] = 0. \quad (42)$$

If the sample length, cavity diameter and length, and the resonant frequency are known, the sample permittivity  $\epsilon'_{rs}$  is the only unknown in (42). However, we cannot solve for  $\epsilon'_{rs}$  explicitly, thus, we employ the Newton–Raphson method to iteratively solve for  $\epsilon'_{rs}$ . Although the Newton–Raphson method requires an initial guess, good convergence occurred even when the initial guess deviated 50% from the sample permittivity for the samples we considered.

TABLE II  
PERMITTIVITY RESULTS FOR FOUR LOW-LOSS DIELECTRIC SAMPLES. THE SAMPLES WERE MEASURED USING BOTH THE SPLIT-CYLINDER RESONATOR AND THE CYLINDRICAL CAVITY. FOR THE SPLIT-CYLINDER RESONATOR, WE SHOW PERMITTIVITY RESULTS USING THE NEW THEORY AND THE THEORY DEVELOPED BY KENT. THE TABLE ALSO SHOWS A COMPARISON BETWEEN SPLIT-CYLINDER RESONATOR AND CYLINDRICAL CAVITY MEASUREMENTS INCLUDING THE COMBINED STANDARD UNCERTAINTIES IN  $\epsilon'_{rs}$

Sample	Split-Cylinder Resonator			Cylindrical Cavity	
	Frequency (GHz)	$\epsilon'_{rs}$ (New theory)	$\epsilon'_{rs}$ (Kent theory)	Frequency (GHz)	$\epsilon'_{rs}$
S9	4.805	$9.82 \pm 0.04$	9.70	9.727	$9.80 \pm 0.05$
S13	4.368	$13.57 \pm 0.05$	13.42	9.717	$13.55 \pm 0.08$
S16	4.131	$16.66 \pm 0.07$	16.49	9.711	$16.64 \pm 0.11$
S20	3.866	$20.87 \pm 0.09$	20.67	9.705	$20.81 \pm 0.16$

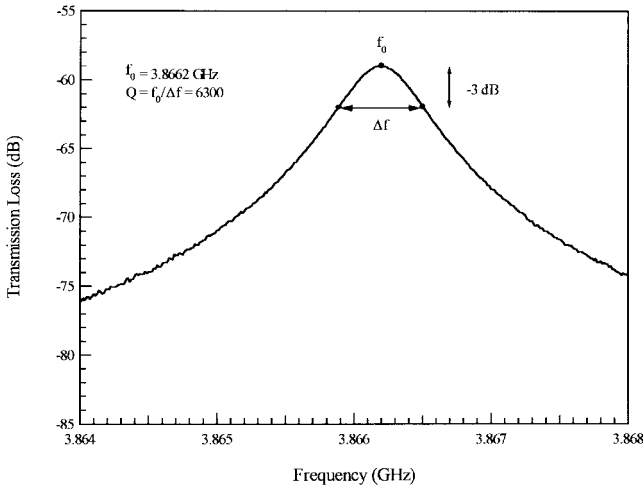


Fig. 4. Typical resonance curve for the split-cylinder resonator.

The theoretical model assumes an infinite number of evanescent  $TE_{0n}$  modes in the cylindrical waveguide regions of the split-cylinder resonator. Practically, we can use only a finite number of  $TE_{0n}$  modes. Table I shows permittivity results for the four samples as a function of the number of  $TE_{0n}$  modes used in the model. For all four samples considered, convergence in  $\epsilon'_{rs}$  is achieved with eight modes in the model.

In order to verify the accuracy of the split-cylinder measurements, we measured the same four samples in a cylindrical resonator [7]. Although the measurements in the cylindrical cavity occur at a slighter higher frequency, the samples are low-loss and the permittivity should be nearly the same. Table II shows good agreement in  $\epsilon'_{rs}$  between the two resonator methods as both measurements of  $\epsilon'_{rs}$  lie within the uncertainty bound of the other.

Table II also shows a comparison between the calculated permittivity of the four samples using both the new split-cylinder theory and the theory developed by Kent [4]. The results using Kent's theory show a consistent downward bias

in the calculation of the sample permittivity. This discrepancy is most likely due to the approximations Kent made in determining the fringing fields in the sample.

Before we can discuss the measurement of the sample loss tangent  $\tan \delta_s$ , we must examine the definition of the quality factor

$$Q = \frac{w(W_c + W_s)}{P_c + P_l + P_s} \quad (43)$$

where  $W_c$  and  $W_s$  are the average energy stored in the cavity sections and sample, and  $P_c$ ,  $P_l$ , and  $P_s$  are the power dissipated per second in the cavity walls, coupling loops, and sample. To evaluate each  $W$  and  $P$  term requires complicated integrations, thus, we make several simplifying approximations. First, as seen in Table IV, the resonance is coupled at a low level, normally below  $-50$  dB. Therefore, we assume that the resistive losses due to the coupling loops are negligible and we neglect  $P_l$ . Also, for the samples we considered, the  $TE_{0n}$  modes in the cylindrical waveguide sections were evanescent. Thus, we also assume  $W_c$  and  $P_c$  are also negligible. With these approximations, (43) reduces to

$$Q \approx \frac{wW_s}{P_s} = \frac{1}{\tan \delta_s}. \quad (44)$$

Thus, we obtain the sample loss tangent by taking the inverse of the measured quality factor  $Q$ .

To verify the validity of the approximations made in (44), we compared the loss-tangent measurements made in the split-cylinder resonator to those made in the cylindrical cavity. From Table III, we find good agreement between the two methods for all four samples. This confirms our hypothesis that a majority of the electromagnetic energy is stored in the sample and almost all of the power is dissipated within the sample.

As with the case of the sample permittivity, Table III shows a comparison of loss-tangent measurements of the four samples using the method described above and the theory developed by Kent. The agreement between the two methods

$$\Delta \epsilon'_{rs} = \sqrt{\left[ \frac{\partial \epsilon'_{rs}}{\partial a} \Delta a \right]^2 + \left[ \frac{\partial \epsilon'_{rs}}{\partial L} \Delta L \right]^2 + \left[ \frac{\partial \epsilon'_{rs}}{\partial d} \Delta d \right]^2 + \left[ \frac{\partial \epsilon'_{rs}}{\partial f_0} \Delta f_0 \right]^2} \quad (45)$$

TABLE III  
LOSS-TANGENT RESULTS FOR FOUR LOW-LOSS DIELECTRIC SAMPLES. THE SAMPLES WERE MEASURED USING BOTH THE SPLIT-CYLINDER RESONATOR AND THE CYLINDRICAL CAVITY. FOR THE SPLIT-CAVITY RESONATOR, WE SHOW LOSS-TANGENT RESULTS USING THE NEW THEORY AND THE THEORY DEVELOPED BY KENT. THE TABLE ALSO SHOWS A COMPARISON BETWEEN SPLIT-CYLINDER RESONATOR AND CYLINDRICAL CAVITY MEASUREMENTS INCLUDING THE COMBINED STANDARD UNCERTAINTIES IN  $\tan \delta_s$

Sample	Split-Cylinder Resonator			Cylindrical Cavity	
	Frequency (GHz)	$\tan \delta_s$ (New theory)	$\tan \delta_s$ (Kent theory)	Frequency (GHz)	$\tan \delta_s$
S9	4.805	$(2.8 \pm 0.6) \times 10^{-4}$	$3.0 \times 10^{-4}$	9.727	$(2.5 \pm 3) \times 10^{-4}$
S13	4.368	$(1.4 \pm 0.3) \times 10^{-4}$	$1.2 \times 10^{-4}$	9.717	$(1.1 \pm 1) \times 10^{-4}$
S16	4.131	$(0.8 \pm 0.2) \times 10^{-4}$	$0.8 \times 10^{-4}$	9.711	$(0.4 \pm 4) \times 10^{-4}$
S20	3.866	$(1.6 \pm 0.3) \times 10^{-4}$	$1.4 \times 10^{-4}$	9.705	$(2.0 \pm 1) \times 10^{-4}$

TABLE IV  
ERROR SOURCES AND THEIR CONTRIBUTIONS TOWARDS THE COMBINED STANDARD UNCERTAINTY IN  $\epsilon'_{rs}$  FOR SAMPLE S20

Parameter		$\Delta$ Parameter	$\Delta\epsilon'_{rs}$
Cylindrical Waveguide Radius	a = 19.09 mm	0.05 mm	0.069
Cylindrical Waveguide Length	L=15.22 mm	0.05 mm	0.002
Sample Thickness	d=3.39 mm	0.01 mm	0.051
Resonant Frequency	$f_0=3.8659$ GHz	0.0005 GHz	0.011

is good, and the results using the Kent theory fall well within the uncertainty bounds of the method described in this paper.

## V. UNCERTAINTY ANALYSIS

The uncertainty in  $\epsilon'_{rs}$  includes errors due to the cavity length and diameter, sample length, and resonant frequency. We assume that each of these error sources are independent. The combined standard uncertainty  $\Delta\epsilon'_{rs}$  is shown in (45), at the bottom of the previous page.

Solutions to the partial derivatives in (45) were found numerically. Table IV shows the error sources along with their contribution to the combined standard uncertainty in  $\epsilon'_{rs}$  for one of the samples measured. The largest contributions of uncertainty come from the uncertainty in the cylindrical waveguide radius and sample thickness. One should note that the uncertainty in sample thickness was only 10  $\mu\text{m}$  due to some sample machining. For materials without any sample machining, one should expect the uncertainty in sample thickness to be significantly higher and to be the largest source of measurement uncertainty for  $\epsilon'_{rs}$ . The uncertainties for all the samples are shown in Table II and are on the order of those found with in the cylindrical cavity.

In calculating the loss tangent  $\tan \delta_s$ , we made several simplifying approximations, which made the loss tangent calculable from the measured quality factor  $Q$ . If we neglect the systematic uncertainties introduced by these simplifying approximations, we can calculate the uncertainty in  $\tan \delta_s$  from the uncertainty in the measured  $Q$ . For these sets of measurements, we assume a 10% uncertainty in measured  $Q$  [7]. The combined standard uncertainties in  $\tan \delta_s$  that result are shown in Table III. The uncertainties in the cylindrical

cavity are higher because the losses in the cavity walls are significant and cannot be neglected.

## VI. CONCLUSIONS

Prior to this paper, the analysis of the split cylinder has been based on a perturbation calculation to approximate the fringing fields in the sample. Although the perturbation calculation provided relatively accurate measurements, there remained some systematic error in the determination of the sample permittivity. The full-wave analysis presented in this paper removes this systematic error by properly taking into account the fringing fields in the sample region outside of the cylindrical waveguide sections.

Using this model, we measured the sample permittivity  $\epsilon'_{rs}$  for four low-loss ceramic samples. For comparison, we measured the same samples in a cylindrical resonator and found good agreement between the two sets of measurements. We also include measurements of the sample loss tangent  $\tan \delta_s$  derived from measurements of the split-cylinder resonator quality factor. These values also compare well with those taken in a cylindrical cavity.

## ACKNOWLEDGMENT

The authors thank G. Kent and E. Kuester for their insightful comments and suggestions.

## REFERENCES

- [1] J. Baker-Jarvis, R. Geyer, J. Grosvenor, M. Janezic, C. Jones, B. Riddle, C. Weil, and J. Krupka, "Dielectric characterization of low-loss materials in the range 1–20 GHz: A comparison of techniques," *IEEE Trans. Dielect. Elect. Insulation*, vol. 5, pp. 571–577, Aug. 1998.
- [2] G. Kent, "An evanescent-mode tester for ceramic dielectric substrates," *IEEE Trans. Microwave Theory Tech.*, vol. 36, pp. 1451–1454, Oct. 1988.
- [3] —, "Nondestructive permittivity measurement of substrates," *IEEE Trans. Instrum. Meas.*, vol. 45, pp. 102–106, Feb. 1996.
- [4] G. Kent and S. Bell, "The gap correction for the resonant-mode dielectrometer," *IEEE Trans. Instrum. Meas.*, vol. 45, pp. 98–101, Feb. 1996.
- [5] J. Baker-Jarvis, M. Janezic, P. Domich, and R. Geyer, "Analysis of an open-ended coaxial probe with lift-off for nondestructive testing," *IEEE Trans. Instrum. Meas.*, vol. 43, pp. 711–718, Oct. 1994.
- [6] J. Baker-Jarvis and M. Janezic, "Analysis of a two-port flanged coaxial holder for shielding effectiveness and dielectric measurements of thin films and thin materials," *IEEE Trans. Electromag. Compat.*, vol. 38, pp. 67–70, Feb. 1996.
- [7] E. Vanzura, R. Geyer, and M. Janezic, *The NIST 60-Millimeter Diameter Cylindrical Cavity Resonator: Performance for Permittivity Measurements*, NIST Standard TN-1354, 1993.



**Michael D. Janezic** (S'93–M'95) received the B.S. degree in electrical engineering, the Masters degree from the University of Colorado at Boulder, in 1991 and 1996, respectively, and is currently working toward the Ph.D. degree in electrical engineering with a specialization in electromagnetic theory.

Since 1988, he has worked with the Radio Frequency Technology Division, National Institute of Standards and Technology, Boulder, CO. His research interests include complex permittivity measurements of bulk and thin-film materials.



**James Baker-Jarvis** (M'89–SM'90) was born in Minneapolis, MN. He received the B.S. degree in mathematics and the M.S. degree in physics from the University of Minnesota at Minneapolis-St. Paul, in 1975 and 1980, respectively, and the Ph.D. degree in theoretical physics from the University of Wyoming, Laramie, in 1984.

Following graduation, he was an AWU Post-Doctoral Fellow for one year, involved with theoretical and experimental aspects of intense electromagnetic fields in lossy materials and dielectric measurements. He then spent two years as a temporary Assistant Professor in the Physics Department, University of Wyoming, where he was involved with electromagnetic heating processes, maximum-entropy techniques, taught classes, and performed research on electromagnetic propagation in lossy materials. Until 1988, he was an Assistant Professor of physics at North Dakota State University. In January 1989, he joined the National Institute of Standards and Technology (NIST), Boulder, CO, where his interests are in the areas of materials, dielectric and magnetic spectroscopy, and nondestructive evaluation. He has authored numerous publications in such diverse areas as dielectric and magnetic measurements, electromagnetics, kinetic theory of fracture, hydrodynamics, heat transfer, maximum-entropy methods, and numerical modeling.

Dr. Baker-Jarvis was a recipient of an NIST Bronze Medal.